THE MECHANICS OF INTERFACE FRACTURE IN LAYERED COMPOSITE MATERIALS: (6) SPALLATION OF THERMAL BARRIER COATINGS OF TURBINE BLADES

Bo Yuan[1], Christopher M. Harvey[1], Rachel C.Thomson[2], Gary W. Critchlow[2] and Simon S. Wang[1,3]

[1] Department of Aeronautical and Automotive Engineering, Loughborough University, Loughborough, Leicestershire LE11 3TU, UK
E-mails: s.wang@lboro.ac.uk, c.m.harvey@lboro.ac.uk

[2] Department of Materials Engineering, Loughborough University, Loughborough, Leicestershire LE11 3TU, UK
E-mails: r.c.thomson@lboro.ac.uk, g.w.critchlow@lboro.ac.uk

[3] School of Mechanical and Equipment Engineering, Hebei University of Engineering, Handan, China

Keywords: Engine turbine blades, Pocket energy concentration, Spallation, Thermal barrier coating

ABSTRACT

It is consensus that local spallation failures in thermal barrier coatings (TBCs) are determined synergistically by many factors. The present experimental test results confirm a completely new spallation failure mechanism for the electron beam-physical vapour deposited (EB-PVD) TBCs on engine turbine blades, which is hypothesized in the latest work [1, 2] for the study of thin film spallation. That is, the spallation is driven by pockets of energy concentration (PEC). This paper reports the experimental study.

1 INTRODUCTION

Thermal barrier coatings (TBCs) are typically applied on gas or aero turbine engines. They protect components from high and prolonged heat loads, therefore improve the durability and energy efficiency of engines [3]. In general, the yttria-stablized zirconia (YSZ) ceramic top coat is bonded on the metallic substrate by either an overlay or diffusion bond coat. During thermal exposure, a layer of thermally grown oxide (TGO) is generated and this is regarded as a critical contributing factor to interfacial damage in TBCs [4-6].

TBCs fabricated by the electron beam-physical vapour deposition (EB-PVD) technique have longer service life comparing with that of air-plasma sprayed (APS) TBCs. This is due to the relatively higher strain tolerance resulting from the columnar structure. Therefore, EB-PVD TBCs are particularly effective in controlling the coating thickness and tailoring microstructures for in-plane modulus. Nevertheless, the research identified that spallation failure in the EB-PVD TBCs was one of the most common interfacial damages [5, 6], which was caused by the cracking at the TGO/metal interface. Numerous experimental observations showed that TBC fractures were synergistically determined by many factors, and different models were proposed accounting for different dominant factors, such as sintering [7], oxidation [8], adhesion degradation [9], thermal stress due to the mismatch of coefficients of thermal expansion [10], creep [11] and interfacial undulation geometry [12] etc. However, in terms of experimental approach, most samples were small pieces that were cut from blades and out of real curved geometry, which may re-distribute the stress features in the whole multi-layer system. In addition, new minor cracks at layer interfaces may be induced during the sample preparation. As for the analytical approach, it still lacks comprehensive physical explanation of the coating spallation procedure, from the blister nucleation to eventually kink-off.

Recently, Wang and Harvey et al [1, 2] developed a mechanical model, which hypothesized that pockets of energy concentration (PECs) existed due to dynamic and non-uniform plastic relaxation or creep in the film such as TBC and substrate during cooling, and would be the driving energy for constant room temperature spallation failure. Experimental studies were carried out in the present study to investigate the spallation mechanics of EB-PVD TBCs that with γ/γ' bond coat, including the separation nucleation, stable and unstable growth, and final spallation at the interface between the TGO and the bond coat. To avoid the cutting effects mentioned above, whole blades were used in the present experiment.

2 MECHANICAL MODEL [1, 2]

Fig. 1 ketches a circular separation blister of radius R_B of TBC with thickness h and the subscript B representing the edge of the blister.

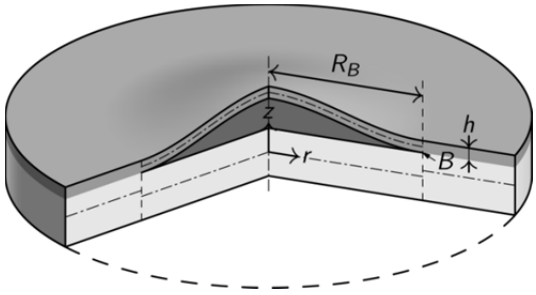

Figure 1: A sketch of a circular TBC blister of radius R_B.

The blister shape is assumed to be sinusoidal and axisymmetric,

$$w(r)=\frac{A}{2}\left[1+\cos\left(\frac{\pi r}{R_B}\right)\right] \tag{1}$$

with w representing the upward deflection and A is the amplitude or the maximum separation. The blister energy at growth is expressed in

$$\left(U_a\right)_{GR}=\pi R_B^2 G_c\left\{\frac{3}{2}+\frac{6\bar{\varepsilon}_0}{\pi^2}\left(\frac{R_B}{h}\right)^2\left[\frac{3}{\pi^2\varphi_0}\left(\frac{R_B}{h}\right)^2-1\right]\right\} \tag{2}$$

where $\bar{\varepsilon}_0=\sigma_0\left(1-\nu^2\right)/E=\sigma_0/\bar{E}$ is the residual plane strain with σ_0 representing the biaxial compressive residual stress, and $\varphi_0=h\sigma_0/G_c$. E, ν are the Young's modulus and Poison's ratio of the TBC material, and G_c is the interface fracture toughness. For the nucleation of the blister, the PEC needs to provide the blister energy $\left(U_a\right)_{GR}=3\pi R_B^2 G_c/2$. After nucleation, the blister grows slowly until it reaches the characteristic buckling radius. Then, unstable growth starts at

$$\left(\frac{R_B}{h}\right)_{UG}^2=\frac{\pi^2\varphi_0}{12}\left[1-\left(1-\frac{\alpha^2}{\Omega}\right)^{1/2}\right] \tag{3}$$

where $\Omega=\bar{\varepsilon}_0\varphi_0/2=h{\sigma_0}^2/\left(2\bar{E}G_c\right)$, is the ratio between the residual plane strain energy density and the interfacial fracture toughness, and UG represents the unstable growth. It is worth noting that the characteristic buckling here is different from the bifurcation type buckling used in the conventional approach for buckling driven delamination in which the amplitude A of the blister is zero at the instant of buckling. However, the amplitude A of the blister here is of a finite value and hence it is expected that the non-bifurcation type buckling occurs well before the bifurcation type buckling. The

parameter α in Eq. (3) is introduced to take account of the effect of amplitude A which can be considered an initial imperfection. In the work [1, 2], α is considered an effect of boundary conditions. Its range is therefore $0.652 \le \alpha \le 1.220$ with the two limits corresponding to simply-supported and clamped edge conditions respectively. The interface fracture toughness G_c decreases with service time increasing, leading to larger Ω. Therefore, the value of Ω is generally much larger than α^2, i.e. $\Omega >> \alpha^2$. Then, the Eq. (3) becomes

$$\left(\frac{R_B}{h}\right)^2_{UG} = \frac{(\alpha\pi)^2}{12\bar{\varepsilon}_0} \tag{4}$$

The violent unstable growth rapidly enlarges the size of the blister which can cause either blister top cracks or spallation at the edges. The spallation radius is calculated as

$$\left(\frac{R_B}{h}\right)^2_{SP} = \frac{\pi^2\varphi_0}{6}\left\{1-\left[1-\frac{3}{2\Omega}\right]^{1/2}\right\} \tag{5}$$

with SP representing spallation. From Eq. (6), it is seen that Ω has to be larger than 3/2 for spallation to occur. When $\Omega >> 3/2$, Eq. (6) becomes

$$\left(\frac{R_B}{h}\right)^2_{SP} = \frac{\pi^2}{4\bar{\varepsilon}_0} \tag{6}$$

The above equations can be equally applied for either classical plate partition theory [13-16] or first-order shear-deformable plate partition theory [13-16] or 2D elasticity plate partition theory [17-19]. However, the interface fracture toughness G_c needs to be taken as $G_c = G_{Ic}$, $G_c = 4\psi G_{Ic}/(3+\psi)$ and $G_c = \psi G_{Ic}/(0.3773 + 0.6227\psi)$ respectively for the three partition theories, where G_{Ic} is the critical mode I fracture toughness and $G_{IIc} = \psi G_{Ic}$.

3 EXPERIMENTS

3.1 Experimental method

The specimen is the first-stage blade from a high-pressure turbine provided by Rolls-Royce PLC. It includes a single crystal CMSX-4 Ni-based superalloy substrate, and a Pt-diffusion bond coat. The α-alumina dominated oxides are generated between the bond coat and top coat during heating.

The specimen was isothermally oxidised in a furnace at 1135°C, and then cooled to the room temperature in the laboratory condition. This heating-cooling cycle was repeated until the convex surfaces failed. To accelerate the surface failing, water was applied to the convex surfaces of the specimen. The cooling, room-temperature moistening, and failing process were recorded by the digital camera, and the recording speed is 30 frames per second. The time values were counted from when the specimen is out of the furnace.

The YSZ top coat has an average Young's modulus of 30–40 GPa [19, 20]. The TGO's Young's modulus is around 380–400 GPa [21], and its thickness is 2–5 μm [20-22]. From the SEM observation of the spalled pieces in the present study, it is confirmed that spallation occurred at the interface between the TGO and the bond coat. Moreover, the thickness of the top coat and the TGO were found to be 138 μm and 5 μm respectively. For the present preliminary study, an equivalent Young's modulus for the combined TBC and TGO thin layer is calculated by equating the effective in-plane stiffness in the radial direction, i.e. $E_{TBC}h_{TBC} + E_{TGO}h_{TGO} = E(h_{TBC} + h_{TGO}) = Eh$. Taking $E_{TBC} = 40\,\text{GPa}$ and $E_{TGO} = 400\,\text{GPa}$ gives the value of the equivalent Young's modulus as $E = 52.587\,\text{GPa}$. The Poisson's ratio is assumed to be 0.22. The compressive residual stress was generated in the temperature difference of 1110°C, and the typical thermal expansion mismatch between the top coat

and the Ni-substrate is 4 ppm/°C. The mode-I interfacial fracture toughness is 8.4 J/m^2 at the interface between the TGO and bond coat [22] and the fracture toughness ratio ψ is taken to be 5 [23].

3.2 Experimental comparison

For the whole blade, the first thermal duration was 100 hrs, with repeated thermal cycles of 20 hrs thereafter. Water was sprayed on the blade convex surface after the 1st cycle (100 hrs) and after 2nd cycle (+20 hrs) but not after subsequent cycles. The convex surface spalled after 12 thermal cycles (total 220 hrs of heating). No spallation failures appeared during cooling, but the convex surface of the blade spalled shortly after its temperature had dropped to the lab temperature at constant residual stress. The specimen was cooled in the furnace room, which has low humidity; therefore, the effect of moisture is negligible.

Fig. 2 shows a sequence of optical and processed images for a blister development including nucleation, stable growth and unstable growth on the convex surface. Image (a) was set as the reference image in the compound subtract processing of images (b) to (d). Although the present image-processing technique is unable to capture the nucleation stage, there is a small spot in (b), which is just discernible (circled in red), which can be regarded as the nucleation. It is seen that the size of this spot is much smaller than the buckling radius of 2.15 mm that is usually assumed in the conventional buckling approach from Eq. (4) with $\alpha = 1.22$ (see Table 1 as well). For nucleation, the PEC needs to provide the blister energy $(U_a)_{GR} = 3\pi R_B^2 G_c/2$ as given in Eq. (2). After nucleation, the blister grew steadily to the radius ~ 1.1 mm as shown in (c). The steady growth took about 1 s. It is worth noting that the nucleation and steady growth are driven by PEC. After the steady stage, an unstable growth occurred. It grew to the size shown in (d) within 1 frame from (c), i.e. 1/30 s. This unstable growth is driven by both PEC and buckling. Although the blister is not a standard circular blister in (d), it is seen the right-half circle in (d) was developed from the circular blister in (c) and the radius was measured to be 2.5 mm.

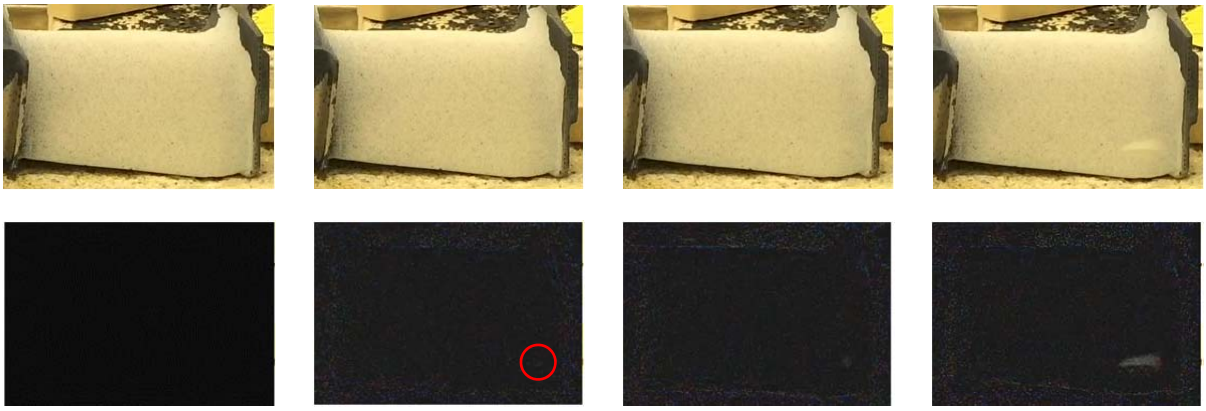

(a) 50 min 19 s, 0th frame (as ref) | (b) 50 min 20 s, 14th frame | (c) 50 min 21 s, 13rd frame | (d) 50 min 21 s, 14th frame

Figure 2: Sequence of optical and processed images showing the nucleation (b), stable growth (b-c) and unstable growth (c-d) of a blister on the EB-PVD TBC convex surface.

Fig. 3 shows the subsequent optical and processed images for further unstable growth, branching and spallation of the blister. Image (a) in Fig. 2 was used again as the reference image in the compound subtract processing of images (e) to (h) in Fig. 3. Images (e) to (g) in Fig. 3 show the further unstable growth of the blister, which was still driven by PEC and buckling. The radius of the right-half circle of the blister in (e) was 2.8 mm. After 1/30 s, the blister branched as shown in image (f); however, the right-half blister remained circular with radius about 2.8 mm. Following that, the blister continued its unstable growth both in the branching directions and the right-half circular

direction. The right-half circle radius in (g) was measured as 3.1 mm. Ridge cracks were also observed in (g). After about 1 s, both the blister and ridge cracks extended again and the radius of the right-half circle was measured as 3.3 mm. 12 s after image (h), the branches extended very rapidly and detached from the substrate. The blister radius just prior to this was still 3.3 mm, and is regarded as the spallation radius.

Analytical predictions and experimental results from previous observations are compared in the following. First, the parameter Ω is determined, $\Omega_{CP}=13.802$, $\Omega_{SP}=5.521$, and $\Omega_{2D}=9.636$, with CP, SP and 2D representing classical plate partition theory, first-order shear-deformable plate partition theory, and 2D elasticity plate partition theory, respectively. It is seen that all the three values are larger than α^2 required by Eq. (3) and 1.5 required by Eq. (5). Then, the Eqs. (3) and (4) are used to predict the initiation of the blister unstable growth, and Eqs. (5) and (6) are to predict the spallation radius. The results are recorded in Table 1. It is seen that the radius of the initiation for the unstable growth from experimental observation is very close to the analytical prediction when taking $\alpha=0.652$ and is far smaller than 2.15 mm usually that is assumed in the conventional buckling approach from Eq. (4) with $\alpha=1.22$. Since the values of Ω are much larger than α^2, the Eq. (4) gives good approximation to Eq. (3) as seen from Table 1. This experimental observation clearly confirms the new spallation failure mechanism of thin layer materials which is hypothesized in the latest work [1, 2] for the study of thin film spallation. That is, the spallation is driven by pockets of energy concentration (PEC). It is impressive to see that the predictions for the spallation radius are very close to the experimental result from all the three partition theories.

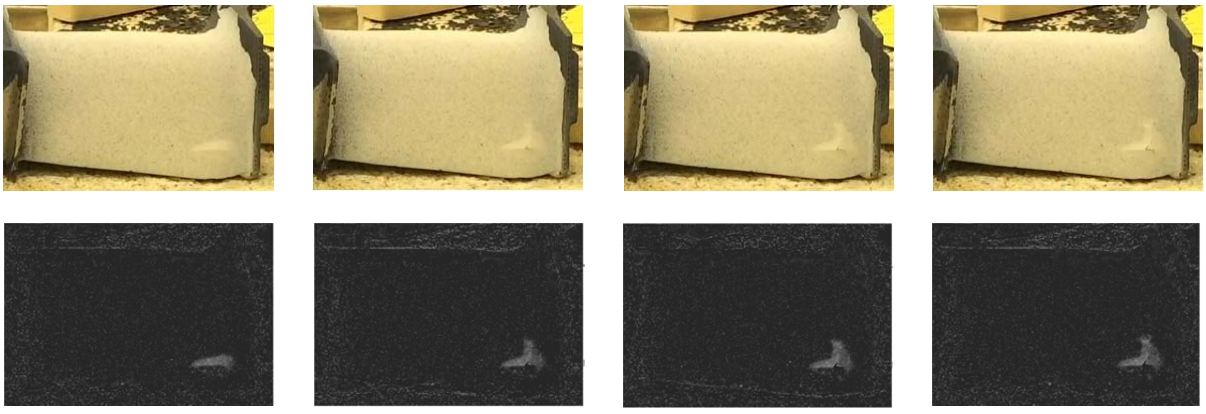

(e) 50 min 21 s, 15th frame (f) 50 min 21 s, 16th frame (g) 50 min 21 s, 20th frame (h) 50 min 22 s, 16th frame

Figure 3: Sequence of optical and processed images showing the further unstable growth, branching and spallation of a blister on the EB-PVD TBC convex surface.

	Unstable growth R_B (mm)					Spallation R_B (mm)				
	Eq. (3)			Eq. (4)		Eq. (5)			Eq. (6)	
α	CP	SP	2D	All	Test data	CP	SP	2D	All	Test data
0.652	1.15	1.16	1.16	1.15						
0.936	1.66	1.68	1.67	1.65	1.1	3.10	3.17	3.12	3.05	3.3
1.22	2.18	2.23	2.19	2.15						

Table 1: Blister radius comparison for unstable growth and spallation.

4 CONCLUSIONS

The coating spallation experiment was carried out to investigate the spallation mechanisms in EB-PVD TBCs, with a Pt-diffusion bond coat. The experimental results are compared to the analytical predictions based on the PECs theory [1, 2] for the preliminary study of the interfacial blister development in EB-PVD TBCs, including nucleation, stable and unstable growth and spallation. It is concluded that the coating blister growth is driven by the blister energy that is supplied by PEC. In the nucleation and stable growth stages the blister is driven by PEC while in the unstable and spallation stages it is driven by both PEC and buckling.

REFERENCES

[1] S. Wang, C.M. Harvey, and B. Wang, Room temperature spallation of α-alumina films grown by oxidation. *Engineering Fracture Mechanics*, available online 14th March 2017 (doi: 10.1016/j.engfracmech.2017.03.002).

[2] C.M. Harvey, B. Wang, and S. Wang, Spallation of thin films driven by pockets of energy concentration. *Theoretical and Applied Fracture Mechanics*, 2017, available on line 21st April 2017 (doi: 10.1016/j.tafmec.2017.04.011).

[3] S. Bose, High temperature coatings, Butterworth-Heinemann, 2011.

[4] T.E. Strangman, Columnar grain ceramic thermal barrier coatings. US4321311 A, 1982.

[5] N.P. Padture, M. Gell, and E.H. Jordan, Materials science - Thermal barrier coatings for gas-turbine engine applications, *Science*, **296**, 2002, pp. 280–284 (doi: 10.1126/science.1068609).

[6] D.R. Clarke and C.G. Levi, Materials design for the next generation thermal barrier coatings, *Annual Review of Materials Research*, **33**, 2003, pp. 383–417 (doi: 10.1146/annurev.matsci.33.011403.113718).

[7] X. Zhao, X. Wang, P. Xiao, Sintering and failure behaviour of EB-PVD thermal barrier coating after isothermal treatment, *Surface & Coatings Technology*, **200**, 2006, pp. 5946-5955 (doi: 10.1016/j.surfcoat.2005.09.006).

[8] L. Rémy, C. Guerre, I. Rouzou, and R. Molins, Assessment of TBC Oxidation-Induced Degradation Using Compression Tests, *Oxidation of Metals*, **81**, 2014, pp. 3–15 (doi:10.1007/s11085-013-9416-9).

[9] P.Y. Thery, M. Poulain, M. Dupeux, M. Braccini, P.Y. Thery, M. Poulain, and M. Dupeux, Spallation of two thermal barrier coating systems: experimental study of adhesion and energetic approach to lifetime during cyclic oxidation, *Journal of Materials Science*, **44**, 2009, pp. 1726–1733 (doi: 10.1007/s10853-008-3108-x).

[10] M. Martena, D. Botto, P. Fino, S. Sabbadini, M.M. Gola, and C. Badini, Modelling of TBC system failure: Stress distribution as a function of TGO thickness and thermal expansion mismatch, *Engineering Failure Analysis*, **13**, 2006, pp. 409–426 (doi: 10.1016/j.engfailanal.2004.12.027).

[11] D.S. Balint, S.S. Kim, Y.F. Liu, R. Kitazawa, Y. Kagawa, and A.G. Evans, Anisotropic TGO rumpling in EB-PVD thermal barrier coatings under in-phase thermomechanical loading, *Acta Materialia*, **59**, 2011, pp. 2544–2555 (doi: 10.1016/j.actamat.2011.01.004).

[12] A.G. Evans, D.R. Mumm, J.W. Hutchinson, G.H. Meier, and F.S. Pettit, Mechanisms controlling the durability of thermal barrier coatings, *Progress in Materials Science*, **46**, 2001, pp. 505–553 (doi:10.1016/S0079-6425(00)00020-7).

[13] S. Wang, C.M. Harvey, A theory of one-dimensional fracture, *Composite Structures*, **94**, 2012, pp. 758–767 (doi: 10.1016/j.compstruct.2011.09.011).

[14] C.M. Harvey and S.Wang, Mixed-mode partition theories for one-dimensional delamination in laminated composite beams, *Engineering Fracture Mechanics*, **96**, 2012, pp. 737–759 (doi: 10.1016/j.engfracmech.2012.10.001).

[15] S. Wang and C.M. Harvey, Mixed mode partition theories for one dimensional fracture, *Engineering Fracture Mechanics*, **79**, 2012, pp. 329–352 (doi: 10.1016/j.engfracmech.2011.11.013).

[16] J.W. Hutchinson and Z. Suo, Mixed Mode Cracking in Layered Materials, *Advances in Applied Mechanics*, **29**, 1991, pp. 63–191 (doi:10.1016/S0065-2156(08)70164-9).

[17] C.M. Harvey, J.D. Wood, S. Wang, and A. Watson, A novel method for the partition of mixed-mode fractures in 2D elastic laminated unidirectional composite beams, *Composite Structures*, **116**, 2014, pp. 589–594 (doi: 10.1016/j.compstruct.2014.05.041).

[18] J.D. Wood, C.M. Harvey, and S. Wang, Partition of mixed-mode fractures in 2D elastic orthotropic laminated beams under general loading, *Composite Structures*, **149**, 2016, pp. 239–246 (doi: 10.1016/j.compstruct.2016.04.016).

[19] E.P. Busso, Z. Qian, M.P. Taylor, and H.E. Evans, The influence of bondcoat and topcoat mechanical properties on stress development in thermal barrier coating systems. *Acta Materialia*, **57**, 2009, pp. 2349–2361 (doi: 10.1016/j.actamat.2009.01.017).

[20] D. Liu, C. Rinaldi, and P.E.J. Flewitt, Effect of substrate curvature on the evolution of microstructure and residual stresses in EBPVD-TBC, *Journal of the European Ceramic Society*, **35**, 2015, pp. 2563–2575 (doi: 10.1016/j.jeurceramsoc.2015.02.024).

[21] J.S. Wang and A.G. Evans, Measurement and analysis of buckling and buckle propagation in compressed oxide layers on superalloy substrates, *Acta Materialia*, **46**, 1998, pp. 4993–5005 (doi: 10.1016/S1359-6454(98)00172-4).

[22] X. Zhao, J. Liu, D.S. Rickerby, R.J. Jones, and P. Xiao, Evolution of interfacial toughness of a thermal barrier system with a Pt-diffused γ/γ′ bond coat, *Acta Materialia*, **59**, 2011, pp. 6401–6411 (doi: 10.1016/j.actamat.2011.07.001).

[23] N.A. Fleck, A.C.F. Cocks, and S. Lampenscherf, Thermal shock resistance of air plasma sprayed thermal barrier coatings, *Journal of the European Ceramic Society*, **34**, 2014, pp. 2687–2694 (doi: 10.1016/j.jeurceramsoc.2014.01.002).